

Chemistry A European Journal

 **Chemistry
Europe**
European Chemical
Societies Publishing

Accepted Article

Title: High Efficiency Sky-Blue Gold(III)-TADF Emitters

Authors: Dongling Zhou, Gang Cheng, Glenna So Ming Tong, and Chi-Ming Che

This manuscript has been accepted after peer review and appears as an Accepted Article online prior to editing, proofing, and formal publication of the final Version of Record (VoR). This work is currently citable by using the Digital Object Identifier (DOI) given below. The VoR will be published online in Early View as soon as possible and may be different to this Accepted Article as a result of editing. Readers should obtain the VoR from the journal website shown below when it is published to ensure accuracy of information. The authors are responsible for the content of this Accepted Article.

To be cited as: *Chem. Eur. J.* 10.1002/chem.202003855

Link to VoR: <https://doi.org/10.1002/chem.202003855>

WILEY-VCH

FULL PAPER

High Efficiency Sky-Blue Gold(III)-TADF Emitters

Dongling Zhou,^[a] Gang Cheng,^{*,[a,b,c]} Glenna So Ming Tong,^{*,[a]} and Chi-Ming Che^{*,[a,b,c]}

[a] Dr. D. Zhou, Dr. G. Cheng, Dr. G. S. M. Tong, Prof. Dr. C.-M. Che
State Key Laboratory of Synthetic Chemistry, HKU-CAS Joint
Laboratory on New Materials, Department of Chemistry,
The University of Hong Kong
Pokfulam Road, Hong Kong SAR (China)
E-mail: ggcheng@hku.hk; tongsm@hku.hk; cmche@hku.hk

[b] Dr. G. Cheng, Prof. Dr. C.-M. Che
Centre of Machine Learning for Energy Materials and
Devices, The University of Hong Kong
Pokfulam Road, Hong Kong SAR (China)

[c] Dr. G. Cheng, Prof. C.-M. Che
HKU Shenzhen Institute of Research and Innovation
Shenzhen (China)

Supporting information for this article is given via a link at the end of the document.

Abstract: Highly efficient sky-blue luminescent gold(III) complexes with emission quantum yields up to 82%, lifetimes down to 0.67 μ s and emission peak maxima at 470–484 nm were prepared through a consideration of pincer gold(III) donor-acceptor complexes. Photo-physical studies and time-dependent density functional theory (TDDFT) calculations revealed that the emission nature of these gold(III) complexes is most consistent with TADF. Solution-processed OLEDs with these gold(III) complexes as dopants afforded electroluminescence maxima at 465–473 nm with FWHM of 64–67 nm and maximum external quantum efficiencies (EQEs) of up to 15.25%. This research demonstrates the first example of gold(III)-OLEDs showing electroluminescence maxima at smaller than 470 nm, and highlights the potential of using gold(III)-TADF emitters in the development of high efficiency blue OLEDs and blue emissive dopant in WOLEDs.

Introduction

Due to the low-lying d orbitals of gold(III) ion, the emissive excited states of phosphorescent gold(III) complexes are usually dominated by long-lived ligand-centered triplet excited states (³IL), with emission lifetimes being hundreds of microseconds^[1] which accounts for large efficiency roll-offs in organic light-emitting diodes (OLEDs) based on phosphorescent Au(III) emitters.^[1d,j-l] The year 2017 marks a great leap in the development of gold(III) OLED emitters, in which luminescent gold(III) complexes showing efficient thermally activated delayed fluorescence (TADF) with high quantum yields approaching unity and short lifetimes of < 2 μ s have been realized; these luminescent parameters are comparable to those of ³MLCT-(MLCT = metal-to-ligand charge transfer) or mixed ³IL/³MLCT-emitting Ir(III)/Pt(II) phosphors.^[2,3] More importantly, recent works on OLEDs fabricated with tetradentate gold(III)-TADF emitters showed maximum external quantum efficiencies (EQEs) of up to 25% and long operational lifetimes (LT₉₅) of 5280 h at 100 cd m⁻².^[3b] These recent findings underpin the competitiveness of gold(III)-TADF emitters among the most efficient metal phosphors of Ir^{III} and Pt^{II}.

While phosphorescent green- and red-emitting materials for use in OLED industry are mature, the development of efficient and stable blue phosphors remains a challenging task. Besides

the stringent requirements on designing complexes with high emission energy that avoids deactivating ligand-to-metal charge transfer (LMCT) or d-d ligand field excited states, high emission quantum yields with short exciton lifetimes are also critical parameters of the metal phosphors used in fabricating blue OLEDs with long operational lifespan. Although purely organic blue TADF emitters have been reported, most of the as-fabricated devices showed high efficiency roll-off with the device lifetime far from satisfactory owing to the singlet-triplet and triplet-triplet annihilation caused by the relatively long triplet excited state lifetime of organic compounds (milliseconds to seconds). In this regard, the design of blue gold(III)-TADF emitters is an appealing approach. Organogold(III) complexes with emission color towards the blue spectral region have been reported in the literature; for instance, in 2017, Venkatesan and co-workers reported gold(III) complexes constructed with NHC-containing C[∧]C chelates that show vibronic-structured emission with maxima locating at ~380–480 nm.^[4] Yam and co-workers also reported blue gold(III) phosphors with photoluminescence maxima at ~470–500 nm and electroluminescence maxima at ~480–500 nm.^[1k-l, 5] However, vibronically structured ³IL excited states of gold(III) complexes have long emission lifetimes (tens to hundreds of microseconds), thus rendering these complexes unsuitable for the fabrication of OLEDs with practical interest. In our previous work in 2017,^[2] a green-emitting gold(III)-TADF complex (a5 in Figure 1) with emission maximum at 524 nm in toluene solution at room temperature was used to fabricate OLEDs that showed sky-blue emission peak at 486 nm with Commission Internationale de L'Eclairage (CIE) coordinates of (0.21, 0.42) and maximum EQEs of 15.7%. This encouraging result prompted us to prepare blue gold(III)-TADF emitters.

As a TADF emitter, the dominant emission comes from the S₁ excited state. From our previous work, the S₁ excited state of complex a5 is predominantly derived from the HOMO → LUMO transition where the HOMO is localized on the aryl donor triphenylamine (TPA) and the LUMO is localized mainly on the C[∧]N[∧]C ligand (Figure 1), and hence, of ligand-to-ligand charge transfer (LLCT) character. Thus, to blue-shift the TADF emission of complex a5 to realize blue gold(III)-TADF emitter, either lowering the HOMO energy of the aryl donor or raising the LUMO energy of the C[∧]N[∧]C ligand could increase the S₁ energy to the blue region. Two sky-blue gold(III) complexes (1 and 2 in Figure 1) were thus prepared by replacing the OEt group in complex a5

FULL PAPER

with a more electron-donating dimethylamine (NMe_2) group to raise the LUMO energy; for **2**, the phenyl rings of the TPA donor were further substituted with electron-withdrawing fluoride to lower the HOMO energy. Complex **3** with no substituents at the pyridine moiety of the $\text{C}^{\wedge}\text{N}^{\wedge}\text{C}$ ligand was also prepared for comparison. It was found that **1** and **2** show good performance when used as an emissive dopant for fabrication of blue OLED with maximum EQE as high as 15.25% as well as WOLED device showing maximum EQE of 13.35%, suggesting that $\text{Au}(\text{III})$ -TADF complexes could emerge to become a new class of luminescent metal dopants for high efficiency blue OLEDs with potential practical interest.

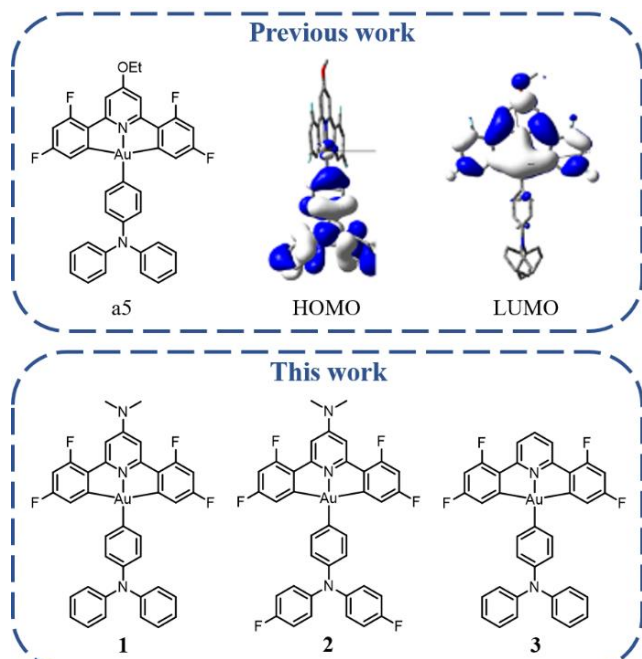


Figure 1. Top: Previously reported arylgold(III)-TADF complex **a5**^[2] and its HOMO and LUMO surfaces. Bottom: donor-acceptor type $\text{C}^{\wedge}\text{N}^{\wedge}\text{C}$ gold(III) complexes **1–3** in this work.

Results and Discussion

X-ray crystallography

A diffraction-quality crystal of **3** was obtained by slow evaporation of a fluorobenzene solution of this complex. Its structure determined by X-ray crystal analysis is depicted in Figure S1 and selected bond lengths/angles are tabulated in Table S1. The gold atom of this complex adopts a slightly distorted square-planar geometry with the C–Au–C angle of $\text{Au}(\text{C}^{\wedge}\text{N}^{\wedge}\text{C})$ and the N–Au–C (ancillary ligand) angle being $161.40(15)^\circ$ and $176.32(12)^\circ$, respectively. The Au–C bond distances within the $\text{Au}(\text{C}^{\wedge}\text{N}^{\wedge}\text{C})$ unit [$2.051(4)$ – $2.069(4)$ Å] are slightly longer than the Au–C (ancillary ligand) bond distance [$2.016(3)$ Å] and the Au–N bond distance is $2.033(3)$ Å. The Au-bound phenyl ring of the N-substituted ancillary ligand (TPA) is not coplanar with the $\text{Au}(\text{C}^{\wedge}\text{N}^{\wedge}\text{C})$ plane, making a dihedral angle of 61.36° . All of these structural features are akin to those of the reported $(\text{C}^{\wedge}\text{N}^{\wedge}\text{C})\text{–Au}^{\text{III}}$ aryl complexes.^[2] The molecules of **3** are packed in a head-to-tail fashion throughout the crystal structure with inter-planar distances of approximately 3.2–3.5 Å (Figure S1).

Electrochemistry

The cyclic voltammograms of **1–3** in *N,N*-dimethylformamide (DMF) were recorded with 0.1 mol dm^{-3} [$n\text{Bu}_4\text{N}$] PF_6 as supporting electrolyte and saturated calomel electrode (SCE) as the reference electrode (Figure S2). A reversible reduction couple was observed at $E_{1/2}$ of -1.71 to -1.70 V for **1** and **2** but at a much less negative $E_{1/2}$ of -1.37 V for **3** (Table 1); this reduction couple is thus attributed to the reduction of $\text{C}^{\wedge}\text{N}^{\wedge}\text{C}$ ligands,^[2,3a] with LUMO energy (E_{LUMO}) being -2.67 eV for **1** and **2** and -3.02 eV for **3** (Table 1). When compared with complex **a5** ($E_{\text{LUMO}} = -2.85$ eV) which bears an OEt substituent on the pyridine moiety of the $\text{C}^{\wedge}\text{N}^{\wedge}\text{C}$ ligand, it is evident that changing the OEt substituent to more electron-donating NMe_2 to form **1** and **2** substantially increases the LUMO energy, and the LUMO of **1** and **2** is 0.35 eV higher-lying than that of the unsubstituted complex **3**. A quasi-reversible oxidation couple was observed at $E_{\text{pa}} = 0.94$ V for **1** and **3** with HOMO energy (E_{HOMO}) being ca. -5.16 eV and at $E_{\text{pa}} = 0.97$ V for **2** with E_{HOMO} being -5.19 eV (Table 1). These oxidation couples are assigned to the oxidation of the TPA donor,^[2,3a] the fluorine substituents at the TPA ligand thus slightly lower the HOMO energy by ca. 0.03 eV.

Photophysical properties

The UV-vis absorption and emission spectra of **1–3** in toluene solutions are shown in Figure 2a, and the corresponding photophysical data are tabulated in Table 1. Complexes **1–3** showed intense absorption bands at ~ 300 nm ($\epsilon = (3\text{--}5) \times 10^4 \text{ dm}^3 \text{ mol}^{-1} \text{ cm}^{-1}$), and moderately intense absorption bands at $330\text{--}390$ nm ($\epsilon = (4\text{--}27) \times 10^3 \text{ dm}^3 \text{ mol}^{-1} \text{ cm}^{-1}$); these intense absorption bands are assigned to metal-perturbed $^1\pi\text{--}\pi^*$ transitions (^1IL) of the $\text{C}^{\wedge}\text{N}^{\wedge}\text{C}$ ligand.^[2] Additional weak absorption bands/tails at ca. $380\text{--}430$ nm with $\epsilon = (1\text{--}4) \times 10^3 \text{ dm}^3 \text{ mol}^{-1} \text{ cm}^{-1}$ were observed, which are assigned to be derived from metal-perturbed $^1(\pi(\text{TPA}) \rightarrow \pi^*(\text{C}^{\wedge}\text{N}^{\wedge}\text{C}))$ LLCT transition.^[2] Upon photo-excitation, all three complexes display structureless emission bands (Figure 2a) with k_r on the order of $10^5\text{--}10^6 \text{ s}^{-1}$ and emission lifetimes of < 1 μs . Complexes **1** and **2** display sky-blue emission at 495 and 483 nm with high emission quantum yields of 0.81 and 0.60 , respectively. As a reference, complex **3**, which does not have electron-donating substituent at the pyridine moiety, has the emission peaked at 566 nm with a high emission quantum yield of 0.93 and a short lifetime of 0.84 μs . Thus, introducing an NMe_2 substituent on **3** to give **1** leads to a blue shift in emission maximum by $\sim 2500 \text{ cm}^{-1}$ (~ 0.31 eV), close to the LUMO energy shift of 0.35 eV as estimated from the electrochemical data. The incorporation of F substituents at the TPA ligand in **2** leads to a further blue shift of $\sim 500 \text{ cm}^{-1}$ (~ 0.06 eV), which is also comparable to the HOMO energy change of ~ 0.03 eV estimated from CV measurements. Thus, our present approach in blue-shifting the emission band from the green to the blue region is valid and it gives support to the proposition that the emission is derived from a $\text{HOMO} \rightarrow \text{LUMO}$ LLCT excited state. The charge transfer nature of the emissive excited state is further corroborated by emission measurements in different polarity solvents. Complex **1** has been chosen as a representative example. As depicted in Figure 2b, an increase in solvent polarity leads to a conspicuous red shift of 45 nm ($\sim 1680 \text{ cm}^{-1}$) in emission maxima. The Lippert-Mataga plot of **1** indicates a large positive slope of 11555 cm^{-1} (Figure 2c), supporting that the emissive excited state of **1** has significant charge transfer character.

FULL PAPER

Table 1. Photophysical and electrochemical properties of complexes 1–3.

Complex	Absorption λ_{abs} [nm] ($\epsilon \times 10^3$ [dm ³ mol ⁻¹ cm ⁻¹]) ^[a]	Emission ^[b]		E_{pa} [V]; ^[c] E_{HOMO} [eV] ^[d]	$E_{1/2}^{\text{red}}$ [V]; E_{LUMO} [eV] ^[d]
		In toluene λ_{em} [nm] (Φ [%]; τ [μ s]; $k_f \times 10^5$ [s ⁻¹])	In PMMA thin films λ_{em} [nm] (Φ [%]; τ [μ s]; $k_f \times 10^5$ [s ⁻¹])		
1	301(44.98), 333(25.25), 347(14.79), 361(6.49), 386(br, 3.87)	495 (0.81; 0.68; 11.9)	484 (0.82; 0.97; 8.5)	0.94; -5.16	-1.71; -2.67
2	300(53.59), 332(27.61), 346(20.28), 361(10.12), 386(br, 4.56)	483 (0.60; 0.67; 9.0)	470 (0.34; 0.95; 3.6)	0.97; -5.19	-1.70; -2.67
3	302(33.70), 354(3.83), 372(5.27), 390(5.17), 430(br, 1.45)	566 (0.93; 0.84; 11.1)	550 (0.81; 0.69; 11.7)	0.94; -5.15	-1.37; -3.02

[a] In degassed toluene (2×10^{-5} mol dm⁻³) at room temperature. "br" stands for broad. [b] Emission quantum yields in toluene and PMMA were measured under the excitation wavelength at 386 nm (for 1 and 2) and 430 nm (for 3) with Hamamatsu C11347 Quantaurus-QY Absolute PL quantum yields measurement system. Samples for thin films were made with 4 wt% of gold(III) complex doped in PMMA. [c] Potentials versus SCE; E_{pa} refers to anodic peak potential for quasi-reversible oxidation wave. [d] Estimated from oxidation ($E_{\text{onset}}^{\text{ox}}$) and reduction ($E_{\text{onset}}^{\text{red}}$) potentials based on $E_{\text{HOMO/LUMO}} = -[4.8 + (E_{\text{onset}}^{\text{ox/red}} \text{ versus ferrocene } E_{1/2})]$ eV; the potentials $E_{1/2}$ of ferrocene lie in the range of 0.49–0.50 V.

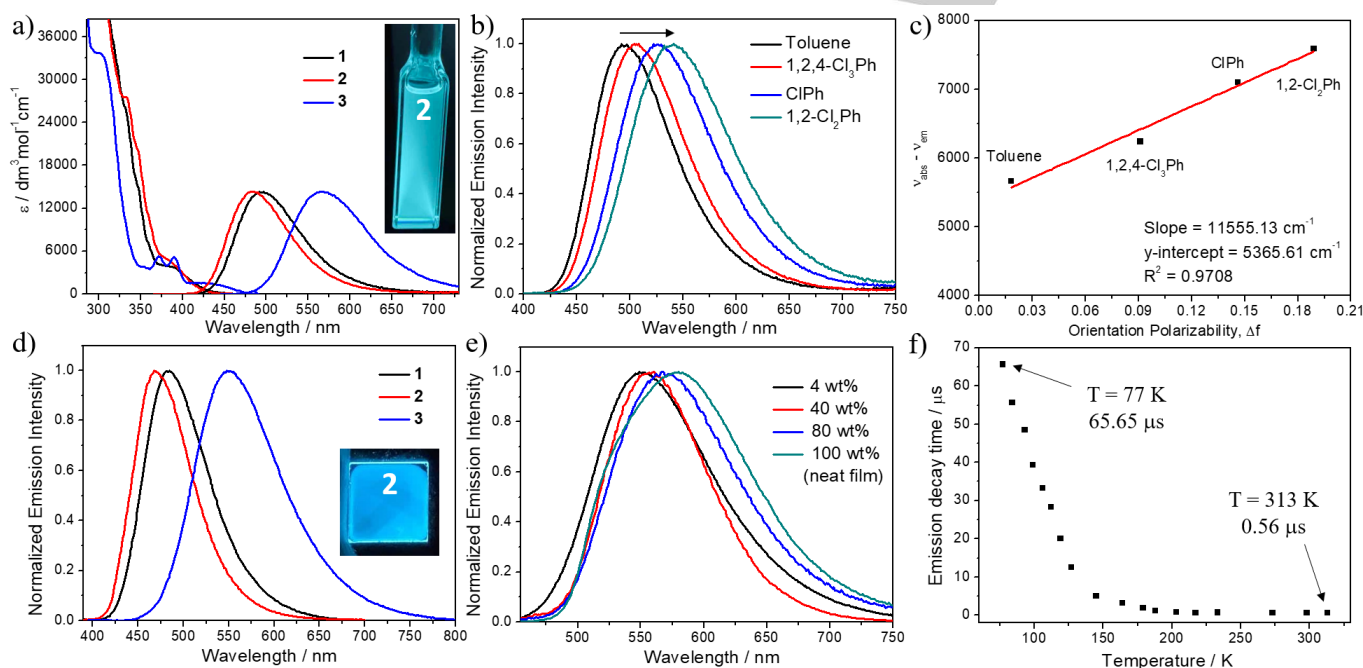


Figure 2. a) Absorption and emission spectra of 1–3 in degassed toluene; inset: the photo of 2 in degassed toluene under 365 nm excitation. b) Emission spectra of 1 in different deoxygenated solvents. c) The Lippert-Mataga plot of 1. d) Emission spectra of 1–3 in PMMA thin films; inset: the photo of 2 in PMMA thin film under 365 nm excitation. e) Emission spectra of 3 doped in PMMA thin films with different concentrations and in neat film at room temperature. f) Emission lifetimes of 1 plotted versus temperature.

The emissions of these complexes doped in poly(methyl methacrylate) (PMMA) thin films with 4 wt% doping concentration (Figure 2d) show emission profiles similar to those in toluene solutions and maintain high Φ of up to 0.82 and short τ of less than 1 μ s; only 2 showed an obvious decrease in emission quantum yield from 0.60 in toluene solution to 0.34. It is particularly noteworthy that the full width at half maximum (FWHM) of the emission band for 1 and 2 is only 82 and 74 nm, respectively. The emission properties of 3 in PMMA thin films with different concentrations and in neat film have also been studied since this complex shows appealing intermolecular interaction in its crystal packing (Figure 3e, *vide infra*). As depicted in Figure 2e, the emission maxima are progressively red-shifted from 550 nm (4

wt%) to 580 nm (100 wt%; neat film). Such red-shifted emission maxima might be presumably due to the aggregation arising from π - π stacking between adjacent (C^N^C)-Au^{III} planes. Similar aggregation-induced red-shifted emission in PMMA thin films has also been reported for a pyrazine-containing C^N^C gold(III) complex.^[1h] However, different from the reported gold(III) complex featuring aggregation-induced enhancement in emission quantum yields, complex 3 shows concentration-dependent photoluminescence quenching from 81% (in 4wt% thin film) to 10% (in neat film). For a comparison, the emission of 1 and 2 in thin films with different doping concentrations was also examined (Figure S7 and Table S3). With increased doping concentration in PMMA matrix, both 1 and 2 showed red-shifted emission maxima

FULL PAPER

by 17–26 nm and obvious aggregation-induced emission quenching, similar to the behavior of **3**.

Since the photo-physical behaviors of **1–3** in solutions are similar to the previously reported Au(III) complexes,^[2, 3] it is speculated that the emission of the complexes studied herein is also derived from TADF. In order to further elucidate the emission mechanism of these complexes, we have performed emission measurements in aerated toluene solution at room temperature (Table S3). Compared to the emission in oxygen-free toluene, the emission quantum yields of **1–3** in aerated toluene are found to decrease substantially (by 96–97%), indicating that triplet excited states are involved in the emission process. The study of variable-temperature emission lifetimes was carried out for **1** in toluene over the temperature range of 313–77 K. As depicted in Figure 2f, the emission lifetimes slowly increase from 313 to 150 K and below 150 K, there is a dramatic increase in radiative lifetime which reaches 65.65 μs at 77 K, together with a more than 2 orders of magnitude decrease in k_r ($8.23 \times 10^3 \text{ s}^{-1}$ at 77 K as compared to $1.27 \times 10^6 \text{ s}^{-1}$ at 313 K). The significant change in k_r from $\sim 10^6 \text{ s}^{-1}$ at RT to $\sim 10^3 \text{ s}^{-1}$ thus implies that the emission mechanism involves thermal activation with the higher-lying excited state having k_r at least two orders of magnitude faster than the lower-lying excited state. Typical vibronic-structured emission bands with vibrational spacings of 1050–1380 cm^{-1} and the order of k_r being 10^3 s^{-1} , recorded at 77 K, together suggest that the emission at 77 K predominantly stems from the $^3\text{IL}(\text{C}^*\text{N}^*\text{C})$ excited state.^[1b, 1f]

Computational study

In the literature, there are two proposed thermally activated emission mechanism that involves triplet excited state in the emission process: (1) TADF, where the higher-lying states with faster k_r is the singlet excited state and the low-lying state is the triplet excited state; and (2) thermally stimulated phosphorescence,^[6] where the higher-lying excited state is also a triplet excited state but has a much faster k_r and is thermally accessible. To help differentiate the two mechanisms, DFT/TDDFT computations were performed on **1** as an illustrative example. From TDDFT optimizations of the triplet excited states, there are two close-lying triplet excited states that are thermally accessible, the $^3\text{IL}(\text{C}^*\text{N}^*\text{C})$ and the $^3\text{LLCT}$ excited states with the adiabatic triplet excited state energy being 2.81 and 2.78 eV, respectively. For both triplet excited states, owing to their little metal character involved (<12%), the computed phosphorescence radiative decay rate constants are of the order 10^3 s^{-1} (Table S7), which are almost three orders of magnitude smaller than the observed k_r (Table 1); thus, it is unlikely that the emission mechanism involves thermally stimulated phosphorescence as there is no low-lying triplet excited state that has $k_r > 10^6 \text{ s}^{-1}$. On the other hand, the $^1\text{LLCT}$, i.e., the S_1 excited state, is only $\sim 500 \text{ cm}^{-1}$ above the $^3\text{LLCT}$ excited state at the optimized $^3\text{LLCT}$ geometry and the radiative decay rate constant for $^1\text{LLCT} \rightarrow \text{S}_0$ is of the order 10^7 s^{-1} ; when TADF is invoked as the emission mechanism (assuming Boltzmann statistics, see eq. (S1) in the Supporting Information), the computed k_r is $1.71 \times 10^6 \text{ s}^{-1}$. Given that the computed vertical emission energies of the $^1\text{LLCT}$ and $^3\text{LLCT}$ excited states at their respective optimized excited state geometry are ~ 491 and 482 nm , respectively, both the computed emission energy and the radiative decay rate constant are in good agreement with the experimental value of 495 nm in toluene solution at RT, thus showing that TADF is the

emission mechanism most consistent with the experimental observations.

Aggregation of pincer Au^{III}-TADF complexes

The study of the emission of complex **3** doped in thin films with different concentrations suggests the feasibility that intermolecular interactions lead to red-shift in emission energy upon aggregation. To further investigate the aggregation properties of the complex, emission measurement was conducted in a mixed solvent system (acetone/water). Complex **3** is non-emissive in pure aerated acetone at room temperature. Upon addition of water into acetone with increasing water fraction (f_w) from 60% to 90%, the emission intensity of **3** showed conspicuous enhancement (from 7% to 26%) with a concomitant emission color change from yellow to orange-red (Figure 3a inset and 3b). As shown in Table S5, the k_r values of the complex in aerated acetone-water mixtures are approximately 10^5 s^{-1} , comparable to that in deoxygenated toluene solution. A slight increase in Φ from 26% to 30% was observed upon degassing the solution (f_w : 90%) of **3**. Obvious red-shifted vibronic absorption bands were observed in solutions with f_w of 60–90% compared to the absorption spectrum recorded in pure acetone solution (Figure 3c). The complex in a mixed acetone-water system (f_w : 60–90%) was subjected to nanoparticle tracking analysis (NTA) revealing the formation of nanoparticles as depicted in Figure S8.

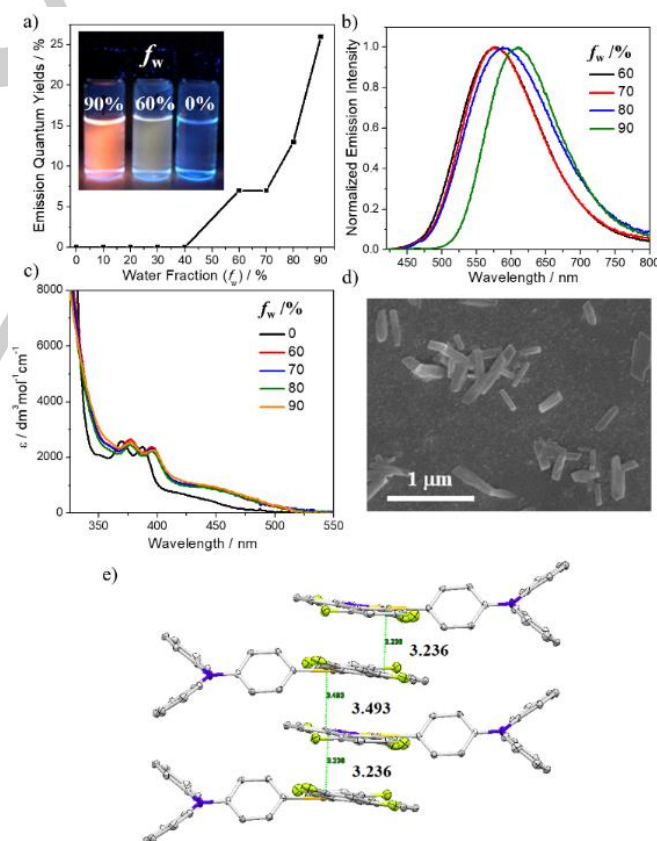


Figure 3. a) Plots of emission quantum yields versus f_w of **3**; inset: Photos of **3** in pure aerated acetone and acetone-water mixtures under 365 nm excitation. b) PL spectra of **3** in acetone-water mixtures with different f_w . c) Absorption spectra of **3** in acetone with different water contents. d) SEM image of nanostructures obtained from **3** in acetone/ H_2O (1:9, v/v). e) Crystal packing of **3** with intermolecular contacts of 3.2–3.5 Å.

FULL PAPER

The SEM image of **3** in acetone-water (1:9, v/v) also showed the formation of self-assembled particles in the nanoscale regime (Figure 3d). Aggregation-induced red-shifted vibronic absorption bands were also reported in other (C^NN^C)-Au^{III} complexes.^[7] Since **3** is insoluble in water, molecules would aggregate upon addition of water, presumably driven by intermolecular interactions between the Au(C^NN^C) planes as revealed in the crystal packing (Figure 3e). The enhancement of emission quantum yield upon increasing water content is possibly due to the increased population of aggregated species (Figure S8). Since the absorption energies of the complex in acetone-water mixtures with f_w of 60–90% are similar (Figure 3c), the observation of red-shifted emission maximum (from 577 to 609 nm; by $\sim 910\text{ cm}^{-1}$) may be due to the stabilization of the charge-transfer excited state in a more polar medium when the water content increases. Considering that **1** and **2**, which contain pincer type Au(C^NN^C) plane similar to that of **3** and also display red-shifted emission induced by the increased concentration in thin films, the aggregation properties of **1** and **2** in acetone-water mixtures ($f_w = 90\%$) were investigated. The observation of red-shifted absorption and the NTA measurement (Figure S9) for **1** and **2** lend support to the formation of nanoparticles upon adding water into their acetone solutions, akin to the case of **3**.

Electroluminescent properties

Solution-processed blue-emitting OLEDs were fabricated by utilizing **1** and **2** as emissive dopants with the device configuration of ITO/PEDOT:PSS/OTPD (4 nm)/PYD2: Au-emitter (60 nm)/DPEPO (10 nm)/TPBi (40 nm)/LiF (1.2 nm)/Al (100 nm). Herein, OTPD [*N,N*-bis(4-(6-((3-ethyloxetan-3-yl)methoxy))hexylphenyl)-*N,N*-diphenyl-4,4'-diamine] underwent cross-linking upon annealing after being spin-coated onto the PEDOT:PSS layer from toluene solution.^[8] The ultra-thin OTPD layer facilitated the hole injection to the emissive layer (EML) and prevented the quenching of excitons from the PEDOT:PSS layer; PYD2 [di(9H-carbazol-9-yl)pyridine] served as the host material for **1** or **2** in the EML while DPEPO [bis(2-[di(phenyl)phosphino]phenyl)ether oxide] and TPBi [2,2',2''-(1,3,5-benzinetriyl)tris(1-phenyl-1-H-benzimidazole)] as hole/exciton blocking and electron transporting materials, respectively. Figure 4a shows normalized EL spectra of **1** and **2** at their optimized dopant concentrations (see Figure S13 for the details). The **1**- and **2**-based devices show electroluminescence maxima at 473 and 465 nm, respectively, with FWHM of 64–67 nm and CIE coordinates of (0.16, 0.25) for the former and (0.16, 0.23) for the latter. The color purity of these blue OLEDs is among the best of reported Au(III) complexes and comparable to the best blue gold(I)-TADF emitters, as compared in Table S8,^[1k-1,5,9] and even better than the most widely used phosphorescent Ir(III) and Pt(II) complexes.^[10] Although the color purity of the **1**-based device is not as high as that of the device made with **2**, the maximum EQE of 15.25% shown by the **1**-based device is much higher than that of the **2**-based device (6.76%), because of the higher Φ of emitter **1** in thin films. In the **1**- and **2**-based blue-emitting OLEDs, the host mixture of PVK (polyvinylcarbazole) and OXD-7 [(1,3-bis[(4-*tert*-butylphenyl)-1,3,4-oxadiazolyl]phenylene)] employed in our previously reported Au^{III}-OLEDs was replaced by PYD2 to avoid the quenching of high-energy-emitting **1** and **2** by PVK. In fact, the maximum EQE of **1** (15.25%) in PYD2 is much higher than that in PVK:OXD-7 (7.53%, Figure S14a). The

emission peak maximum of **1** is at 490 nm when PVK:OXD-7 was used as the host (Figure S14b), being red-shifted by 20 nm when compared with that in PYD2 host, leading to a poor color purity with CIE coordinates of (0.19, 0.39). Such red-shifted EL emission could be the result of less confinement of excitons in PVK:OXD-7 host and/or the different polarity of different hosts.

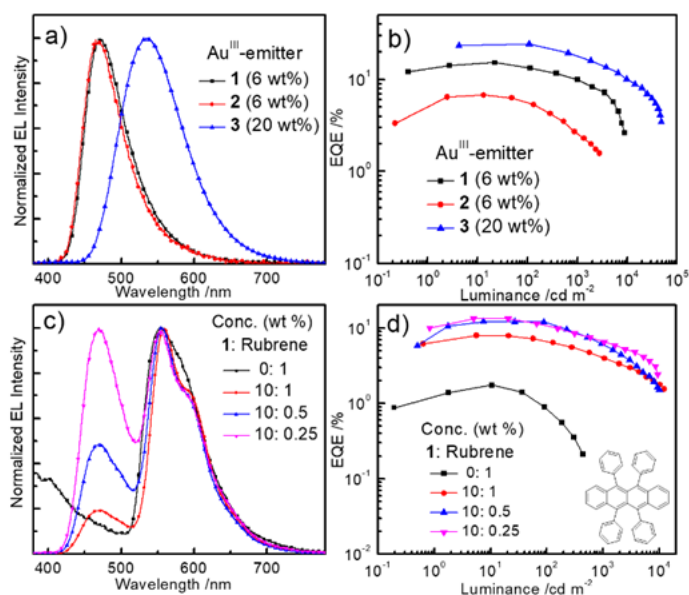
In view of the high Φ achieved by **3**, EL properties of **3** were also investigated in a solution-processed OLED with a structure of ITO/PEDOT:PSS/PVK:OXD-7:3 (60 nm)/TPBi (40 nm)/LiF (1.2 nm)/Al (100 nm). Compared to the configuration of blue-emitting devices, the mixture of PVK and OXD-7 was utilized as the host instead of high-triplet-energy PYD2 with an aim to match the narrower bandgap of **3**; OTPD and DPEPO layers were also removed.^[2] High EQEs of up to 24.32% was found in the green-emitting **3**-based device with EL emission maximum at 534 nm, attributable to the optimized device structure for Au(III)-TADF complexes^[2] and the high Φ of **3** in thin film.

Compared to TADF emitters, traditional fluorescent molecules are more attractive for OLEDs in terms of long-term stability and color purity owing to their much shorter emission lifetimes (\sim ns) and narrower emission spectra. High-efficiency fluorescent OLEDs based on energy down-conversion from phosphorescent or TADF sensitizers to fluorescent emitters have been demonstrated in previous reports.^[11] Nonetheless, most fluorescent OLEDs based on energy down-conversion were fabricated by vacuum deposition, and those fabricated by less expensive solution-processed technique were seldom reported. In this work, we used emitter **1** as the sensitizer and widely used fluorescent molecule rubrene as the emitter to testify the possibility of energy-down-conversion fluorescent OLEDs using a solution-processing technique. The device had a similar structure with the one applied in the **1**-based device described above except that rubrene was introduced in the EML as the fluorescent dopant; ITO/PEDOT:PSS/OTPD (4 nm)/PYD2:1:rubrene (60 nm)/DPEPO (10 nm)/TPBi (40 nm)/LiF (1.2 nm)/Al (100 nm). In the EML of this device, the doping concentrations of **1** and rubrene were 10 and 1 wt%, respectively. For comparison, a regular fluorescent OLED was also fabricated by removing **1** from the EML. As depicted in Figure 4c, the intense host emission in the regular device is suggestive of an inefficient energy transfer from the host to rubrene, leading to poor performance of the device, as shown in Figure 4d. With the addition of sensitizer **1**, the host emission vanished because of the efficient energy transfer from the host to **1**, and the device performance was strongly boosted; maximum luminance and maximum EQEs were respectively increased by 30 and 4.59 times in the energy down-conversion device. Although the residual emission from **1** existed in the down-conversion device, the emission from rubrene dominates the EL spectrum. The enhanced luminance and EQEs could be ascribed to the efficient energy transfer from both singlet and triplet excited states of **1** to rubrene.^[11b] The residual emission from **1**, ascribed to the short emission lifetime of **1**, was detrimental to the color purity of the rubrene-based devices.^[11a,c] Nonetheless, the idea of fabricating a white OLED by combining the blue emission of **1** and orange emission of rubrene may thereby be realized via reducing the concentration of rubrene.^[12] With a 10:0.25 wt% combination of 1:rubrene, white emission with CIE coordinates of (0.32, 0.36) and color rendering index (CRI) of 69.44 was realized with maximum EQE of 13.35% and maximum power efficiency of 21.61 lm W⁻¹.

FULL PAPER

Table 2. Key performance of solution-processed OLEDs based on **1**, **2** and **3**.

Complex (Conc.)	Max Luminance [cd m ⁻²]	Current efficiency [cd A ⁻¹]		Power efficiency [lm W ⁻¹]		External quantum efficiency [%]		CIE (x, y) ^[a]
		Max	at 1000 cd m ⁻²	Max	at 1000 cd m ⁻²	Max	at 1000 cd m ⁻²	
1 (6 wt%)	8850	28.36	18.55	18.46	8.97	15.25	9.98	0.16, 0.25
2 (6 wt%)	2800	12.42	4.72	8.25	1.85	6.76	2.51	0.16, 0.23
3 (20 wt%)	48000	78.16	58.35	93.31	48.95	24.32	18.40	0.35, 0.56

[a] Commission internationale de l'éclairage (CIE) coordinates at 1000 cd m⁻².**Figure 4.** a) Normalized EL spectra and b) EQE-luminance characteristics of solution-processed OLEDs based on **1**, **2** and **3** at their optimized doping concentration. c) Normalized EL spectra and d) EQE-luminance characteristics of solution-processed energy down-conversion fluorescent OLEDs in which **1** and rubrene were both doped in the EML and used as the sensitizer and emitter, respectively.

Conclusion

Sky-blue luminescent arylgold(III)-TADF complexes (**1** and **2**) with emission peak maxima at 470–484 nm in thin films were successfully developed through a strategic consideration of substituent effects on the pincer C^NAC ligand scaffold. These arylgold(III)-TADF complexes show high emission quantum yields of up to 0.82 and lifetimes less than 1 μs. Sky-blue gold(III) TADF OLEDs have been achieved with high EQEs of up to 15.25%, narrow-band emission with FWHM of 64–67 nm (2825–2953 cm⁻¹), and good color purity with CIE coordinates of (0.16, 0.23). A white OLED with CIE coordinates of (0.32, 0.36), CRI of 69.44 and maximum EQE of 13.35% was also successfully fabricated using the down-conversion technique with the combination of the emission from **1** and rubrene. Although the device performance shown by these blue emissive gold(III) complexes still has not met the standard for commercial applications, their high efficiency and the true blue emission color purity altogether indicate the appealing potential of gold(III)-TADF emitters in the future.

development of efficient blue OLEDs and the blue dopants in WOLEDs.

Experimental Section

General

All chemicals, unless otherwise noted, are commercially available and used without further purification. All solvents for the reactions were of HPLC grade. 2,6-Bis(2,4-difluorophenyl)pyridine^[13] and 2,6-bis(2,4-difluorophenyl)-*N,N*-dimethylpyridin-4-amine were prepared by Suzuki coupling reactions between 2,4-difluorophenylboronic acid and 2,6-dibromopyridine/2,6-dibromo-*N,N*-dimethylpyridin-4-amine. (4-(Diphenylamino)phenyl)boronic acid and (4-(bis(4-fluorophenyl)amino)phenyl)boronic acid are commercially available. Particle size distribution was measured using nanoparticle tracking analysis (NTA) instrument PMX 120 ZetaView. The SEM images were taken on scanning electron microscope LEO 1530 FEG operating at 5.00 kV.

X-ray crystallography

A yellow block-shaped crystal of **3** with dimension of 0.39×0.21×0.08 mm³ was mounted on a MiTeGen MicroMount (100-micron aperture) with Dow Corning HVG. The X-ray diffraction data of this crystal were collected on a Bruker D8 VENTURE Fixed-Chi X-ray diffractometer equipped with a Mo Kα (0.71073 Å) radiation, a PHOTON 100 CMOS detector, and an Oxford Cryostream 700 low-temperature device, operating at T = 200(2) K, controlled by using APEX3 software suite v2015.5-2 (Bruker-AXS, 2015). The unit cell was initially determined by the fast Fourier transform method. The frames were integrated with the Bruker SAINT v8.34A (Bruker-AXS, 2013) software package using a wide-frame algorithm. Data were corrected for absorption effects using the Multi-Scan method (SADABS). The ratio of minimum to maximum apparent transmission was 0.403. The structures were solved by using SHELXT 2014/5 software (Sheldrick, 2015) and refined by using SHELXT 2014/7 software.^[14] CCDC 2022575 (for **3**) contains the supplementary crystallographic data for this paper. These data are provided free of charge by The Cambridge Crystallographic Data Centre at <https://www.ccdc.cam.ac.uk>.

Preparation and characterization of gold(III) complexes 1–3

The synthetic protocol of **1–3** is the same as that in the previous studies^[2,15] with the use of cyclometallated gold(III) hydroxides and amino-containing phenylboronic acids. The precursor cyclometallated gold(III) hydroxides [Au(C^NAC)(OH)]^[15] were synthesized using the corresponding cyclometallated gold(III) chlorides^[16] as precursor which were prepared through transmetalation from organomercury chlorides according to the literature. The detailed synthetic procedures and NMR spectra were given in the Supporting Information.

FULL PAPER

2,6-Bis(2,4-difluorophenyl)-*N,N*-dimethylpyridin-4-amine: ^1H NMR (500 MHz, CD_2Cl_2): δ 8.07-8.03 (m, 2H), 7.03-6.99 (m, 2H), 6.97 (s, 2H), 6.95-6.91 (m, 2H), 3.08 (s, 6H); ^{19}F NMR (376 MHz, CDCl_3): δ -110.4, -112.1; ^{13}C NMR (125 MHz, CDCl_3): δ 163.04 (dd, $J = 11.3$, 247.5 Hz), 160.7 (dd, $J = 12.5$, 251.3 Hz), 155.37, 152.59, 132.60, 125.01 (d, $J = 15.0$ Hz), 111.73 (d, $J = 11.3$ Hz), 106.20 (d, $J = 8.8$ Hz), 104.33 (t, $J = 25.0$ Hz), 39.59; HRMS (EI): m/z Calcd. for $\text{C}_{19}\text{H}_{14}\text{F}_4\text{N}_2$ (M^+): 346.1093, found: 346.1058.

1: Yield: 57 mg (48%). ^1H NMR (500 MHz, CD_2Cl_2): δ 7.45 (d, $J = 8.5$ Hz, 2H, H_a), 7.27 (t, $J = 8.5$ Hz, 4H, H_b), 7.14 (d, $J = 8.0$ Hz, 4H, H_i), 7.07-7.04 (m, 4H, H_a, e), 7.00 (t, $J = 7.5$ Hz, 2H, H_h), 6.92 (dd, $J = 2.5$, 7.5 Hz, 2H, H_c), 6.66-6.61 (m, 2H, H_b), 3.16 (s, 6H, $-\text{NMe}_2$); ^{19}F NMR (470 MHz, CD_2Cl_2): δ -109.4, -111.6; ^{13}C NMR (150 MHz, CD_2Cl_2): δ 170.45, 164.03 (dd, $J = 10.5$, 256.9 Hz), 161.70 (dd, $J = 10.5$, 259.5 Hz), 158.72 (d, $J = 6.2$ Hz), 158.04, 148.59, 145.04, 143.00, 134.62, 133.77, 129.51, 126.07, 124.03, 122.53, 117.81 (d, $J = 20.0$ Hz), 102.81 (d, $J = 19.4$ Hz), 102.50 (t, $J = 26.5$ Hz), 40.10; MS (FAB): m/z 785.3 (M^+); Anal. Calcd. (%) for $\text{C}_{37}\text{H}_{26}\text{AuF}_4\text{N}_3$: C 56.57, H 3.34, N 5.35; found: C 57.04, H 3.28, N 5.29.

2: Yield: 51 mg (42%). ^1H NMR (500 MHz, CD_2Cl_2): δ 7.43 (d, $J = 8.5$ Hz, 2H, H_a), 7.12-7.09 (m, 6H, H_a, g), 7.01-6.97 (m, 6H, H_e, i), 6.92 (dd, $J = 2.5$, 7.0 Hz, 2H, H_c), 6.68-6.63 (m, 2H, H_b), 3.20 (s, 6H, $-\text{NMe}_2$); ^{19}F NMR (470 MHz, CD_2Cl_2): δ -107.5, -109.9, -121.6; ^{13}C NMR (150 MHz, CD_2Cl_2): δ 170.00, 163.60 (dd, $J = 9.6$, 256.1 Hz), 161.31 (dd, $J = 10.9$, 259.5 Hz), 158.48 (d, $J = 239.6$ Hz), 158.36, 158.33, 144.82, 144.42 (d, $J = 2.5$ Hz), 142.10, 134.21, 133.38, 125.37 (d, $J = 7.9$ Hz), 124.43, 117.39 (d, $J = 19.1$ Hz), 115.82 (d, $J = 22.4$ Hz), 102.43 (d, $J = 10.0$ Hz), 102.12 (t, $J = 26.6$ Hz), 39.74; ESI-MS: m/z 821.1 (M^+); Anal. Calcd. (%) for $\text{C}_{37}\text{H}_{24}\text{AuF}_6\text{N}_3$: C 54.09, H 2.94, N 5.11; found: C 54.21, H 2.92, N 5.02.

3: Yield: 59 mg (43%). ^1H NMR (500 MHz, CD_2Cl_2): δ 7.98-7.92 (m, 3H, H_a, b), 7.44 (d, $J = 8.5$ Hz, 2H, H_e), 7.28 (t, $J = 7.5$ Hz, 4H, H_b), 7.15 (d, $J = 8.5$ Hz, 4H, H_g), 7.07 (d, $J = 8.5$ Hz, 2H, H_i), 7.01 (t, $J = 7.0$ Hz, 2H, H_i), 6.94 (dd, $J = 2.5$, 7.0 Hz, 2H, H_a), 6.72-6.67 (m, 2H, H_c); ^{19}F NMR (376 MHz, CDCl_3): δ -105.3, -108.7; ^{13}C NMR (150 MHz, CD_2Cl_2): δ 170.80, 164.91 (dd, $J = 10.5$, 258.0 Hz), 161.92 (dd, $J = 10.5$, 259.5 Hz), 160.00 (d, $J = 6.0$ Hz), 148.50, 145.49, 143.32, 141.52, 134.00, 133.21, 129.55, 125.99, 124.20, 122.70, 121.19 (d, $J = 18.0$ Hz), 118.36 (d, $J = 18.0$ Hz), 103.05 (t, $J = 25.5$ Hz); MS (FAB): m/z 742.1 (M^+); Anal. Calcd. (%) for $\text{C}_{35}\text{H}_{21}\text{AuF}_4\text{N}_2$: C 56.62, H 2.85, N 3.77; found: C 56.21, H 2.90, N 3.73.

Photophysical measurements

All solvents for photophysical studies were of HPLC grade, except toluene purified by distillation before photophysical use. Absorption spectra were recorded on a Hewlett-Packard 8453 diode array spectrophotometer at room temperature. Steady-state emission spectra were obtained on a Horiba Fluorolog-3 spectrophotometer. Emission quantum yields (Φ) in solution and thin films were measured with Hamamatsu C11347 Quantaaurus-QY Absolute PL quantum yields measurement system. For absorption and emission measurement, the concentration of the solution is 2×10^{-5} mol dm^{-3} . Solutions for photophysical studies were degassed by using a high vacuum line in a two-compartment cell with five freeze-pump-thaw cycles. The thin-film samples were prepared by drop-cast from a chlorobenzene solution containing 4 wt% of Au^{III} complex with PMMA as hosts. The solvent was evaporated at 80 °C and translucent films were finally obtained. Low-temperature (77 K) emission spectra of complexes in glassy and solid states were recorded in quartz tubes (4 mm internal diameter) placed in a liquid nitrogen Dewar flask with quartz windows. The glassy-state emission of the complex was measured in a mixed solvent system of dichloromethane/methanol/ethanol (1:1:4, v/v/v). The emission lifetime (τ) measurements were performed on a Quanta Ray GCR 150-10 pulsed Nd:YAG laser system. Errors for λ values (± 1 nm), τ ($\pm 10\%$), and Φ ($\pm 10\%$) are estimated.

OLED fabrication

Materials: PEDOT:PSS [poly(3,4-ethylenedioxythiophene):poly(styrene sulfonic acid)] (Clevios P Al 4083) was purchased from Heraeus; OTPD, PVK, OXD-7, PYD2, DPEPO, TPBi, and LiF from Luminescence Technology Corp; Aluminum pellets from Kurt J Lesker. All these materials were used as received and their structural drawings are given in the Supporting Information (Figure S17).

Substrate cleaning: Glass slides with pre-patterned ITO electrodes used as substrates of OLEDs were cleaned in an ultrasonic bath of Decon 90 detergent and deionized water and rinsed with deionized water. Then they were cleaned in sequential ultrasonic baths of deionized water, acetone, and isopropanol, and subsequently dried in an oven for 1 h.

Fabrication and characterization of OLEDs: Aqueous solutions of PEDOT:PSS were spin-coated onto the cleaned ITO-coated glass substrates and baked at 120 °C for 20 min to remove the residual water solvent in a clean room. For blue OLEDs and down-conversion devices, the crosslinkable OTPD was spin-coated on top of the PEDOT:PSS layer and heated at 200 °C for 30 min to carry out crosslinking inside a N_2 -filled glove box. The crosslinked OTPD was then subjected to spin chlorobenzene solvent for three times to remove the unreacted moieties. Afterwards, blends of PYD2: **1** or **2** (for blue OLEDs) or PYD2: **1**: rubrene (for down-conversion devices) were spin-coated from chlorobenzene atop the OTPD layer inside the same N_2 -filled glove box. The thickness for all EMLs was approximately 60 nm. After annealed at 70 °C for 30 min, all devices were subsequently transferred into a Kurt J. Lesker SPECTROS vacuum deposition system without exposing to air. In the vacuum chamber, organic materials of DPEPO and TPBi were thermally deposited in sequence at a rate of 0.1 nm s^{-1} . Finally, LiF and Al were thermally deposited at rates of 0.03 and 0.2 nm s^{-1} , respectively. For the **3**-based OLEDs, the blend of PVK:OXD-7:**3** was directly spin-coated from chlorobenzene atop the PEDOT:PSS layer inside the N_2 -filled glove box. After annealed at 110 °C for 60 min, all devices were subsequently transferred into a Kurt J. Lesker SPECTROS vacuum deposition system without exposing to air. In the vacuum chamber, TPBi was thermally deposited at a rate of 0.1 nm s^{-1} . Finally, LiF and Al were thermally deposited at rates of 0.03 and 0.2 nm s^{-1} , respectively.

Luminance-current-voltage characteristics, CIE coordinates, EL spectra, current efficiency, power efficiency and EQE were measured using a Keithley 2400 source-meter and an absolute external quantum efficiency measurement system (C9920-12, Hamamatsu Photonics). All devices were characterized at room temperature without encapsulation.

Computational details

The hybrid density functional, M06,^[17] was employed for all calculations using the program package G09.^[18] The 6-31G* basis set^[19] is used for all atoms except Au, which is described by the Stuttgart relativistic pseudopotential and its accompanying basis set (ECP60MWB).^[20] Solvent effect was also included by means of the polarizable continuum model (PCM)^[21] and default parameters are used for the solvent, toluene (refractive index $n = 1.4969$). No symmetry constraints were applied in geometry optimizations. For the singlet ground state (S_0), the restricted density functional theory (RDFT) formalism was employed. For the singlet and triplet excited states, TDDFT were employed. Frequency calculations were performed on the optimized structures to ensure that they are minimum energy structures by the absence of imaginary frequency (i.e. $\text{NImag} = 0$). Stability calculations were also performed for all the optimized structures to ensure that all the wavefunctions obtained are stable.

The excited state energies at the optimized excited state geometries were computed using a state-specific approach.^[22] Relative excited state energy gaps were computed using TDDFT within the Tamm-Dancoff approximation (TDA)^[23] to avoid the triplet instability problems.^[24] The radiative decay rate constants, k_r , were computed at the optimized excited

FULL PAPER

state geometries. Detailed procedures for radiative decay rate constant calculations were reported in previous works.^[25] SOC has been included in the computations of triplet radiative decay rate constants.

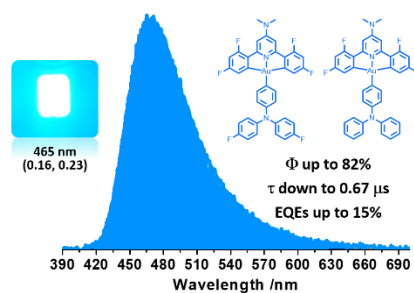
Acknowledgements

This work is supported by the Major Program of Guangdong Basic and Applied Research (2019B030302009), the Basic Research Program of Shenzhen (JCYJ20170818141858021 and JCYJ20180508162429786), Innovation and Technology Fund (PRP/071/19FX), Hong Kong Quantum AI Lab Limited, Hong Kong Research Grants Council (HKU 17330416), and CAS-Croucher Funding Scheme for Joint Laboratories. We thank The University of Hong Kong's University Development Fund for funding the Bruker D8 VENTURE Photon100 CMOS X-Ray Diffractometer. We also thank Dr. K.-H. Low (The University of Hong Kong) for assistance in solving the X-ray crystal structure of complex **3**.

Keywords: Gold • TADF • Sky-Blue OLEDs • WOLEDs • Pincer ligands

- [1] a) W.-P. To, G. S.-M. Tong, W. Lu, C. Ma, J. Liu, A. L.-F. Chow, C.-M. Che, *Angew. Chem. Int. Ed.* **2012**, *51*, 2654-2657; b) W.-P. To, K. T. Chan, G. S. M. Tong, C. Ma, W.-M. Kwok, X. Guan, K.-H. Low, C.-M. Che, *Angew. Chem. Int. Ed.* **2013**, *52*, 6648-6652; c) F.-F. Hung, W.-P. To, J.-J. Zhang, C. Ma, W.-Y. Wong, C.-M. Che, *Chem. Eur. J.* **2014**, *20*, 8604-8614; d) G. Cheng, K. T. Chan, W.-P. To, C.-M. Che, *Adv. Mater.* **2014**, *26*, 2540-2546; e) R. Kumar, A. Linden, C. Nevado, *Angew. Chem. Int. Ed.* **2015**, *54*, 14287-14290; f) W.-P. To, G. S. M. Tong, C.-W. Cheung, C. Yang, D. Zhou, C.-M. Che, *Inorg. Chem.* **2017**, *56*, 5046-5059; g) M. Bachmann, O. Blacque, K. Venkatesan, *Chem. Eur. J.* **2017**, *23*, 9451-9456; h) L. Currie, J. Fernandez-Cestau, L. Rocchigiani, B. Bertrand, S. J. Lancaster, D. L. Hughes, H. Duckworth, S. T. E. Jones, D. Credginton, T. J. Penfold, M. Bochmann, *Chem. Eur. J.* **2017**, *23*, 105-113; i) B. Y.-W. Wong, H.-L. Wong, Y.-C. Wong, V. K.-M. Au, M.-Y. Chan, V. W.-W. Yam, *Chem. Sci.* **2017**, *8*, 6936-6946; j) K. T. Chan, G. S. M. Tong, Q. Wan, G. Cheng, C. Yang, C.-M. Che, *Chem. Asian J.* **2017**, *12*, 2104-2120; k) M.-C. Tang, C.-H. Lee, S.-L. Lai, M. Ng, M.-Y. Chan, V. W.-W. Yam, *J. Am. Chem. Soc.* **2017**, *139*, 9341-9349; l) M.-C. Tang, W.-K. Kwok, S.-L. Lai, W.-L. Cheung, M.-Y. Chan, V. W.-W. Yam, *Chem. Sci.* **2019**, *10*, 594-605.
- [2] W.-P. To, D. Zhou, G. S. M. Tong, G. Cheng, C. Yang, C.-M. Che, *Angew. Chem. Int. Ed.* **2017**, *56*, 14036-14041.
- [3] a) D. Zhou, W.-P. To, Y. Kwak, Y. Cho, G. Cheng, G. S. M. Tong, C.-M. Che, *Adv. Sci.* **2019**, *6*, 1802297; b) D. Zhou, W.-P. To, G. S. M. Tong, G. Cheng, L. Du, D. L. Phillips, C.-M. Che, *Angew. Chem. Int. Ed.* **2020**, *132*, 6437-6444.
- [4] T. von Arx, A. Szentkuti, T. N. Zehnder, O. Blacque, K. Venkatesan, *J. Mater. Chem. C* **2017**, *5*, 3765-3769.
- [5] a) C.-H. Lee, M.-C. Tang, Y.-C. Wong, M.-Y. Chan, V. W.-W. Yam, *J. Am. Chem. Soc.* **2017**, *139*, 10539-10550; b) W.-K. Kwok, M.-C. Tang, S.-L. Lai, W.-L. Cheung, L.-K. Li, M. Ng, M.-Y. Chan, V. W.-W. Yam, *Angew. Chem. Int. Ed.* **2020**, *59*, 9684-9692.
- [6] a) M.-C. Tang, M.-Y. Leung, S.-L. Lai, M. Ng, M.-Y. Chan, V. W.-W. Yam, *J. Am. Chem. Soc.* **2018**, *140*, 13115-13124; b) M.-Y. Leung, M.-C. Tang, W.-L. Cheung, S.-L. Lai, M. Ng, M.-Y. Chan, V. W.-W. Yam, *J. Am. Chem. Soc.* **2020**, *142*, 2448-2459.
- [7] Q. Wan, J. Xia, W. Lu, J. Yang, C.-M. Che, *J. Am. Chem. Soc.* **2019**, *141*, 11572-11582.
- [8] K.-W. Tsai, M.-K. Hung, Y.-H. Mao, S.-A. Chen, *Adv. Funct. Mater.* **2019**, *29*, 1901025.
- [9] a) P. J. Conaghan, S. M. Menke, A. S. Romanov, S. T. E. Hones, A. J. Pearson, E. W. Evans, M. Bochmann, N. C. Greenham, D. Credginton, *Adv. Mater.* **2018**, *30*, 1802285; b) P. J. Conaghan, C. S. B. Matthews, F. Chotard, S. T. E. Jones, N. C. Greenham, M. Bochmann, D. Credginton, A. S. Romanov, *Nat. Commun.* **2020**, *11*, 1-8.
- [10] Y. Im, S. Y. Byun, J. H. Kim, D. R. Lee, C. S. Oh, K. S. Yook, J. Y. Lee, *Adv. Funct. Mater.* **2017**, *27*, 1603007.
- [11] a) M. A. Baldo, M. E. Thompson, S. R. Forrest, *Nature* **2000**, *403*, 750-753; b) H. Nakanotani, T. Higuchi, T. Furukawa, K. Masui, K. Morimoto, M. Numata, H. Tanaka, Y. Sagara, T. Yasuda, C. Adachi, *Nat. Commun.* **2014**, *5*, 1-7; c) P.-K. Chow, G. Cheng, G. S. M. Tong, C. Ma, W.-M. Kwok, W.-H. Ang, C. Y.-S. Chung, C. Yang, F. Wang, C.-M. Che, *Chem. Sci.* **2016**, *7*, 6083-6098.
- [12] G. Cheng, F. Li, Y. Duan, J. Feng, S. Liu, S. Qiu, D. Lin, Y. Ma and S. T. Lee, *Appl. Phys. Lett.* **2003**, *82*, 4224-4226.
- [13] A. J. Wilkinson, H. Puschmann, J. A. K. Howard, C. E. Foster, J. A. G. Williams, *Inorg. Chem.* **2006**, *45*, 8685-8699.
- [14] G. M. Sheldrick, *Acta Crystallogr., Sect. A*, **2015**, *71*, 3-8.
- [15] D.-A. Rosca, D. A. Smith, M. Bochmann, *Chem. Commun.* **2012**, *48*, 7247-7249.
- [16] K.-H. Wong, K.-K. Cheung, M. C.-W. Chan, C.-M. Che, *Organometallics* **1998**, *17*, 3505-3511.
- [17] Y. Zhao, D. G. Truhlar, *Theor. Chim. Acta* **2008**, *120*, 215-241.
- [18] M. J. Frisch, G. W. Trucks, H. B. Schlegel, G. E. Scuseria, M. A. Robb, J. R. Cheeseman, G. Scalmani, V. Barone, B. Mennucci, G. A. Petersson, H. Nakatsuji, M. Caricato, X. Li, H. P. Hratchian, A. F. Izmaylov, J. Bloino, G. Zheng, J. L. Sonnenberg, M. Hada, M. Ehara, K. Toyota, R. Fukuda, J. Hasegawa, M. Ishida, T. Nakajima, Y. Honda, O. Kitao, H. Nakai, T. Vreven, J. A. Montgomery Jr, J. E. Peralta, F. Ogliaro, M. Bearpark, J. J. Heyd, E. Brothers, K. N. Kudin, V. N. Staroverov, R. Kobayashi, J. Normand, K. Raghavachari, A. Rendell, J. C. Burant, S. S. Iyengar, J. Tomasi, M. Cossi, N. Rega, J. M. Millam, M. Klene, J. E. Knox, J. B. Cross, V. Bakken, C. Adamo, J. Jaramillo, R. Gomperts, R. E. Stratmann, O. Yazyev, A. J. Austin, R. Cammi, C. Pomelli, J. W. Ochterski, R. L. Martin, K. Morokuma, V. G. Zakrzewski, G. A. Voth, P. Salvador, J. J. Dannenberg, S. Dapprich, A. D. Daniels, Ö. Farkas, J. B. Foresman, J. V. Ortiz, J. Cioslowski, D. J. Fox, Revision D.01 ed., Gaussian, Inc., Wallingford CT, **2009**.
- [19] a) M. M. Francl, W. J. Petro, W. J. Hehre, J. S. Binkley, M. S. Gordon, D. J. DeFree, J. A. Pople, *J. Chem. Phys.* **1982**, *77*, 3654-3665; b) P. C. Hariharan, J. A. Pople, *Theor. Chim. Acta* **1973**, *28*, 213-222.
- [20] a) D. Andrae, U. Haeusserrmann, M. Dolg, H. Stoll, H. Preuss, *Theor. Chim. Acta* **1990**, *77*, 123-141; b) J. M. L. Martin, A. Sundermann, *J. Chem. Phys.* **2001**, *114*, 3408-3420.
- [21] M. Cossi, G. Scalmani, N. Rega, V. Barone, *J. Chem. Phys.* **2002**, *117*, 43-54.
- [22] a) R. Improta, V. Barone, G. Scalmani, M. J. Frisch, *J. Chem. Phys.* **2006**, *125*, 054103: 054101-054109; b) R. Improta, G. Scalmani, M. J. Frisch, V. Barone, *J. Chem. Phys.* **2007**, *127*, 074504.
- [23] S. Hirata, M. Head-Gordon, *Chem. Phys. Lett.* **1999**, *314*, 291-299.
- [24] a) M. E. Casida, F. Gutierrez, J. Guan, F.-X. Gadea, d. Salahub, J.-P. Daudey, *J. Chem. Phys.* **2000**, *113*, 7062-7071; b) M. J. G. Peach, M. J. Williamson, D. J. Tozer, *J. Chem. Theory Comput.* **2011**, *7*, 3578-3585.
- [25] a) G. S. M. Tong, C.-M. Che, *Chem. Eur. J.* **2009**, *15*, 7225-7237; b) G. S. M. Tong, P. K. Chow, W.-P. To, W.-M. Kwok, C.-M. Che, *Chem. Eur. J.* **2014**, *20*, 6433-6443; c) G. S. M. Tong, K. T. Chan, X. Chang, C.-M. Che, *Chem. Sci.* **2015**, *6*, 3026-3037.

Entry for the Table of Contents



Sky-blue emissive arylgold(III)-TADF complexes with emission maxima at 470–484 nm, Φ of up to 82% and $\tau < 1 \mu$ s were successfully developed through a strategic consideration of substituent effects on the pincer C^NC ligands and triphenylamine donor. Sky-blue emitting OLEDs have been achieved with these gold(III)-TADF emitters, showing high EQEs of up to 15.25%, narrow-band emission and good color purity with CIE coordinates of (0.16, 0.23).